https://doi.org/10.5194/egusphere-2026-152
Preprint. Discussion started: 25 February 2026

Improving Simulations of Zeeman Absorption Spectrum for Hyperspectral Microwave Sounding Applications

Changjiao Dong[1], Fuzhong Weng[2], and Emma Turner[3]

[1]School of Atmospheric Physics, Nanjing University of Information Science and Technology, Nanjing, 210044, China

[2]CMA Earth System Modeling and Prediction Centre (CEMC), China Meteorological Administration, Beijing, 100081, China
[3]European Centre for Medium-Range Weather Forecasts (ECMWF), Reading, RG2 9AX, UK

Correspondence to: Fuzhong Weng (fweng58@gmail.com)

Abstract. Accurate simulation of microwave oxygen absorption is critical for upper atmospheric remote sensing, yet traditional models suffer from biases due to simplified Zeeman splitting calculations. Two key advancements were presented to address this challenge. First, the 2024 RS-LBL model is updated with the Zeeman coefficients of Larsson et al. (2019), which capture higher-order rotational and anisotropic spin effects, thereby eliminating the 1 K bias in 7^+ line simulations caused by the Hund's case (b) approximation. Second, a full vector radiative transfer equation with a complex propagation matrix is implemented to rigorously model polarization under Zeeman splitting, integrated with hybrid Lorentz-Gaussian broadening. Systematic sensitivity experiments quantify the impacts of magnetic field intensity, propagation angle, and frequency shift on polarized brightness temperatures. Leveraging these insights, the Hyperspectral Microwave Atmospheric Sounder (HMAS) is designed: a 60-63 GHz linearly polarized instrument comprising 150 channels, optimized to 39 composite channels for noise reduction. Performance benchmarks against SSMIS UAS channels confirm that HMAS delivers unprecedented vertical resolution with reduced noise, establishing it as an optimal payload concept for next-generation space exploration missions targeting the near space atmosphere.

1 Introduction

Near space typically refers to the region between 20 and 100 km (60-0.0004 hPa) above sea level, encompassing the stratosphere, mesosphere, and lower thermosphere (Yang et al., 2023). Observation of near space is crucial for weather forecasting and climate analysis (Eckermann et al., 2018; Liu et al., 2007; Zhao et al., 2021). The accuracy of upper atmosphere forecasts can be improved by assimilating near space observations in numerical weather prediction (NWP) systems (Eckermann et al., 2009; Hoppel et al., 2013, 2008; Maurer et al., 2015; Nezlin et al., 2009). However, observations of the middle to upper atmosphere are comparatively rare due to technological and scientific limitations (Dong et al., 2024). Satellite-based data used in NWP assimilation systems at altitudes above 1 hPa are typically from the Microwave Limb Sounder (MLS), the Sounding of the Atmosphere using Broadband Emission Radiometry (SABER), and the Special Sensor Microwave Imager/Sounder (SSMIS) on board the Defense Meteorology Satellite Program (DMSP) satellite (Hoppel et al.,

https://doi.org/10.5194/egusphere-2026-152
Preprint. Discussion started: 25 February 2026

2008). The temperature analysis fields from assimilated SSMIS upper atmospheric sounding (UAS) channels are comparable to those from SABER and MLS data (Hoppel et al., 2013). However, SSMIS has only six UAS channels with low vertical resolution and significant noise. Increasing the amount of high-quality upper atmospheric observation data is critical for weather forecasting and climate analysis.

Infrared hyperspectral instruments have now reached maturity, and the radiance data have been proven to improve NWP forecast accuracy (Aires et al., 2015; Eresmaa et al., 2017; Mcnally et al., 2006). However, microwave sensors have significantly fewer detection channels compared to infrared instruments due to technological limitations (Boukabara and Garrett, 2011). With recent advancements in Fast Fourier Transform spectroscopy technology, microwave radiometers with high spectral resolution have become a more feasible component in remote sensing (Kummerow et al., 2022; Liu et al., 2007). This is highly beneficial because microwave hyperspectral sampling can achieve a high-density weighting function (WF), which facilitates the accurate retrieval of temperature and water vapor profiles and exerts a positive impact on weather forecasting (Aires et al., 2015; Zhang et al., 2025). In recent years, various studies have focused on specific hyperspectral microwave channels and their ability to provide valuable observations for retrieval or NWP systems (Bi et al., 2024; Blackwell et al., 2011; Boukabara and Garrett, 2011). However, most studies primarily reference the Advanced Microwave Sounding Unit (AMSU) or Advanced Technology Microwave Sounder (ATMS) temperature and water vapor detection channels (around 52.6-57.3 GHz and 183.31 GHz), which primarily provide information on tropospheric clouds, precipitation, and surface parameters, with limited upper atmospheric information.

Microwave oxygen (O_2) absorption channel observations and simulations above 40 km are affected by Earth's magnetic field. The 2×2 coherency matrix formed radiative transfer equation can describe the Zeeman splitting effect (Lenoir, 1967, 1968; Rosenkranz and Staelin, 1988). To fully investigate the influence of magnetic field parameters on brightness temperature (BT) simulation, Stogryn (1989) derived the magnetic field-related symmetry, systematically revealing the quantitative impact of Zeeman splitting on O_2 absorption line simulations (Stogryn, 1989). However, previous research is based on the Hund's case (b) assumption, which has limitations for low quantum numbers. Larsson et al. (2019) provide a new Zeeman splitting coefficients database, improving the O_2 fine-structure lines simulation accuracy (Larsson et al., 2019). This article provides a brief review of the computational and simulation differences between the Hund's case (b) and Larsson (2019) implementations in Rosenkranz and Staelin's microwave Line-by-Line (referred to as RS-LBL) model (Larsson et al., 2019; Rosenkranz and Staelin, 1988). The RS-LBL model (version 2024) update with Larsson (2019) Zeeman splitting coefficients is employed to analyze the oxygen line sensitivity and detection altitude in section 3. In section 4, the hyperspectral channel characteristics for a microwave sounder capable of high-resolution detecting near space temperature are proposed.

https://doi.org/10.5194/egusphere-2026-152
Preprint. Discussion started: 25 February 2026

2 Microwave Propagation in Near Space O_2 Medium

2.1 Zeeman Splitting Coefficient

Under the influence of an external magnetic field, the Zeeman splitting effect causes energy levels to split, with the emitted or absorbed radiation originating from the molecule's magnetic dipole (Zeeman, 1897). The intensity and direction of the magnetic dipole moment are typically represented by the quantum mechanical matrix element $\mu(N,M,\Delta J,\Delta M)$, which denotes the transition strength when one quantum state transitions to another (Berdyugina and Solanki, 2002; Lenoir, 1968). N represents the molecular quantum number for the end-over-end rotation. The magnetic quantum number M describes the quantum number of the electron's orbital angular momentum (or total angular momentum) component in the direction of a magnetic field within an atom. Its value is related to the total angular momentum quantum number J, expressed as $M=-J,-J+1,\cdots,0,\cdots,J-1,J$, reflecting the spatial orientation of the atomic state within the magnetic field (Hill and Gordy, 1954). ΔJ denotes the total angular momentum quantum number change, describing the alteration in the atom's total angular momentum J before and after the transition. ΔM denotes the difference between the final magnetic quantum number M' and the initial magnetic quantum number M during atomic transitions, i.e., $\Delta M=M'-M$, serving as the core parameter for analyzing molecular radiation behavior and spectral splitting in magnetic fields. It determines the type of transition and directly correlates with the polarization characteristics of the emitted radiation: $\Delta M=0$ is commonly called the π component, $\Delta M=\pm1$ is called the $\sigma^{\pm}$ component (Berdyugina and Solanki, 2002; Lenoir, 1968; Schadee, 1978).

A so-called 'g-factor' is commonly used to quantify the interaction intensity between a magnetic field and specific energy levels J_N of oxygen molecules. In an external magnetic field, g_{J_N} directly determines the energy perturbation of the Zeeman splitting (Hill and Gordy, 1954; Lenoir, 1968):

$$\Delta W=-g_{J_N}\mu_B M_J H \tag{1}$$

where μ_B is the Bohr magneton, H represents the external field strength, M_J is the quantum number for the projection of total angular momentum on the magnetic field direction.

Previous microwave LBL models, such as the Millimeter-Wave Propagation Model (MPM) (Liebe, 1989) and RS-LBL (version 1988) (Rosenkranz and Staelin, 1988), as well as the Atmospheric Radiative Transfer Simulator (ARTS) calculations before 2014 (Larsson et al., 2014), employed Hund's case (b) basis wavefunctions to determine the Zeeman splitting coefficient:

$$g_{J_N}^{\text{Hund\_b}}=\frac{g_S\left[J(J+1)-N(N+1)+S(S+1)\right]}{2J(J+1)} \tag{2}$$

https://doi.org/10.5194/egusphere-2026-152
Preprint. Discussion started: 25 February 2026

where the S is the electronic spin-quantum number. This model is dominated by the electron spin g_S Zeeman effect, neglecting the fine-structure Hamiltonian off-diagonal elements and higher-order Zeeman effects (Larsson et al., 2014; Lenoir, 1968; Rosenkranz and Staelin, 1988).

Recently, (Larsson et al., 2019) provide an updated Zeeman splitting coefficient calculation, which incorporates higher-order rotational g_r and anisotropic spin g_l^e Zeeman effects:

$$g_{J_N}^{\text{Larsson}} = g_S \cos^2\phi + \left(g_S + 2g_l^e\right)\sin^2\phi + 2g_r \cos\phi \sin\phi \tag{3}$$

where ϕ is the diagonalization angle, determined by the ratio of the off-diagonal elements to the diagonal elements in the fine-structure Hamiltonians. For the derivation of the g_S, g_r, g_l^e, and g_{J_N} and the calculation results for $g_{J_N=J-1}$, $g_{J_N=J}$, and $g_{J_N=J+1}$. Please refer to (Larsson et al., 2019).

2.2 Oxygen Absorption

Oxygen absorption at microwave frequencies is a key element in atmospheric remote sensing and retrieval. The frequency characteristics and vertical sounding distribution provide critical data for retrieving atmospheric temperature profiles, pressure profiles, and dynamic processes. In practice, O_2 absorption is not confined to a single frequency of a spectral line but is broadened by other influences (Tretyakov et al., 2005), primarily collisional or pressure broadening in the troposphere, which can typically be represented by Lorentz lines (Koshelev et al., 2015). In the upper atmosphere, the collisional broadening effect diminishes, and the absorption line broadening is now primarily caused by the relative motion of molecules (Doppler broadening), resulting in Gaussian line shapes (Ben-Reuven and Lightman, 1967; Koshelev et al., 2021; Van Vleck and Weisskopf, 1945).

In mathematics, the O_2 absorption coefficient is typically expressed as the per unit volume of oxygen molecules' power absorption efficiency for a specific microwave frequency (Unit: dB/km) (Liebe et al., 1977; Van Vleck, 1947):

$$\alpha(\nu) = n\sum_{j,i} S_{ji}(T)\, F\left(\nu, \nu_{ji}\right) \tag{4}$$

where n is the number of molecules per unit volume, and ν is the incident electromagnetic wave frequency. j and i denote two distinct energy levels of an isolated molecule, where i represents the initial state energy level and j the final state. The absorption or emission process involves the molecule transitioning between energy levels i and j. The corresponding transition frequency is $\nu_{ji} = \left(E_j - E_i\right)/h$, where E_j and E_i are the final and initial states' energy, respectively, h is the Planck constant, $S_{ji}(T)$ the monochromatic intensity of a single molecule at temperature T, $F\left(\nu, \nu_{ji}\right)$ is the normalized line shape function, and the summation term Σ represents the sum over all possible energy level transition combinations.

https://doi.org/10.5194/egusphere-2026-152
Preprint. Discussion started: 25 February 2026

When performing microwave remote sensing and radiative transfer modeling at the atmosphere below 40 km, the O_2 absorption coefficient α is used in the scalar radiative transfer equation to express the absorption and emission of the medium. For this study, oxygen absorption lines above 40 km are also affected by the Zeeman splitting (Hill and Gordy, 1954; Meeks and Lilley, 1963). Only the vector radiative transfer equation can fully describe the radiation polarization characteristics at this complex condition. In the vector radiative transfer equation, the scalar α is replaced by the complex propagation matrix **G**, which incorporates O_2 absorption properties (Lenoir, 1967):

$$\mathbf{G} = \begin{pmatrix} G_{11} & G_{12} \\ G_{21} & G_{22} \end{pmatrix} \tag{5}$$

with

$$G_{11} = \frac{1}{2}\left(1+\cos\theta\right)^2 \cdot G_{\sigma+} + \frac{1}{2}\left(1-\cos\theta\right)^2 \cdot G_{\sigma-} + \frac{1}{2}\left(1-\cos^2\theta\right) \cdot G_{\pi}$$

$$G_{22} = \frac{1}{2}\left(1-\cos\theta\right)^2 \cdot G_{\sigma+} + \frac{1}{2}\left(1+\cos\theta\right)^2 \cdot G_{\sigma-} + \frac{1}{2}\left(1-\cos^2\theta\right) \cdot G_{\pi}$$

$$G_{12} = G_{21} = \frac{1}{2}\left(1-\cos^2\theta\right) \cdot \left(G_{\sigma+} + G_{\sigma-} - G_{\pi}\right)$$

where θ is the angle between the magnetic field vector and the electromagnetic wave propagation direction. The calculation principles and formulas for G_{π}, $G_{\sigma+}$, and $G_{\sigma-}$ are analogous to those in Eq. (4), representing the product of the oxygen Zeeman relative intensities and line shape functions. The O_2 line Zeeman component frequency shift and relative intensity calculation can be found in (Lenoir, 1968). The line shape is calculated using the complex error function (CERROR), as referenced in (Hui et al., 1978).

2.3 Radiative Transfer Transmittance Solution

The g_{J_N} determines the frequency shift and intensity of the oxygen line Zeeman components, influencing the absorption and radiance calculations. Therefore, this study calculates **G** based on both $g_{J_N}^{\text{hund\_b}}$ and $g_{J_N}^{\text{Larsson}}$ and determines the upward radiance. When dealing with the Zeeman effect radiance above 40 km, the BT coherence matrix can be solved directly. Incident radiance is calculated through the scalar radiative transfer model. The BT matrix is a 2×2 matrix, with diagonal elements corresponding to linear-based or circular-based polarized brightness temperatures (Lenoir, 1968).

Alternatively, the total transmittance is calculated based on the oxygen absorption coefficient, and then the BT can be derived. Considering only oxygen absorption, the specific frequency transmittance $\Gamma_{\nu}(z)$ of the O_2 absorption line from

https://doi.org/10.5194/egusphere-2026-152
Preprint. Discussion started: 25 February 2026

altitude z to the top of atmosphere relates to the optical depth τ_ν and O_2 absorption coefficient $\alpha(\nu,z)$ as follows (Meeks and Lilley, 1963; Weng, 2017):

$$\Gamma_\nu(z) = \exp\left(-\frac{\tau_\nu}{\mu}\right) = \exp\left(-\int_z^\infty \frac{\alpha(\nu,z)}{\mu} dz\right) \tag{6}$$

where $\alpha(\nu,z)$ is the volumetric absorption coefficient in unit of cm^{-1}, $\mu = \cos(\beta)$, β is the zenith angle. For atmospheric detection, the integral term in Eq. (6) is obtained by summing all absorptions within each thin layer.

For the atmosphere above 40 km, the product matrix **P** is solved through matrix diagonalization (Rosenkranz and Staelin, 1988). **P** is a 2×2 complex matrix that shares the same properties as **G**. Based on **P**, the transmittance matrix **Γ** can be calculated:

$$\mathbf{\Gamma} = \begin{pmatrix} \Gamma_{VV} & \Gamma_{VH} \\ \Gamma_{HV} & \Gamma_{HH} \end{pmatrix} \tag{7}$$

where the diagonal elements Γ_{VV} and Γ_{HH} represent the vertical and horizontal total transmittance, respectively, while the off-diagonal elements measure the coherence of the diagonal elements. The transmittance within each layer is multiplied by the atmospheric temperature, and then summed across the entire atmospheric column to obtain the brightness temperature matrix.

The relation between the BT matrix diagonal element and the Stokes parameters is:

$$T_{B_{VV}} = (I+Q)/2\,; \quad T_{B_{HH}} = (I-Q)/2\,; \quad T_{B_{VH}} = (U-iV)/2 \tag{8}$$

$$T_{B_{RC}} = (I-V)/2\,; \quad T_{B_{LC}} = (I+V)/2\,; \quad T_{B_{RL}} = (Q+iU)/2 \tag{9}$$

where I is the total radiance intensity, Q is the difference between vertical and horizontal linear polarization, U is the difference between ±45° linear polarization, and V is the difference between left- and right-hand circular polarization (Eriksson et al., 2011).

3 Simulation Results

3.1 Microwave LBL Model Simulations

The BT matrix and Stokes vector for different oxygen absorption lines based on $g_{J_N}^{\text{hund\_b}}$ and $g_{J_N}^{\text{Larsson}}$ are calculated, respectively. Figure 1 shows the Stokes parameter differences between the Hund's case (b) and Larrson (2019) implementations for the different O_2 lines. From Fig. 1, the 7^+ line V component exhibits the greatest absolute BT difference compared to other lines, approaching 1 K at a frequency shift of 1.3 MHz. The absolute differences of the 1^- oxygen line in I,

https://doi.org/10.5194/egusphere-2026-152
Preprint. Discussion started: 25 February 2026

Q, and V exceed 0.5 K within a frequency shift of 1 MHz. The differences are significant, and the newer Zeeman spectroscopy will hopefully improve the representation of upper atmosphere observations. Overall, the U component simulation differences of all oxygen lines are minimal, while the I and V components are more pronounced.

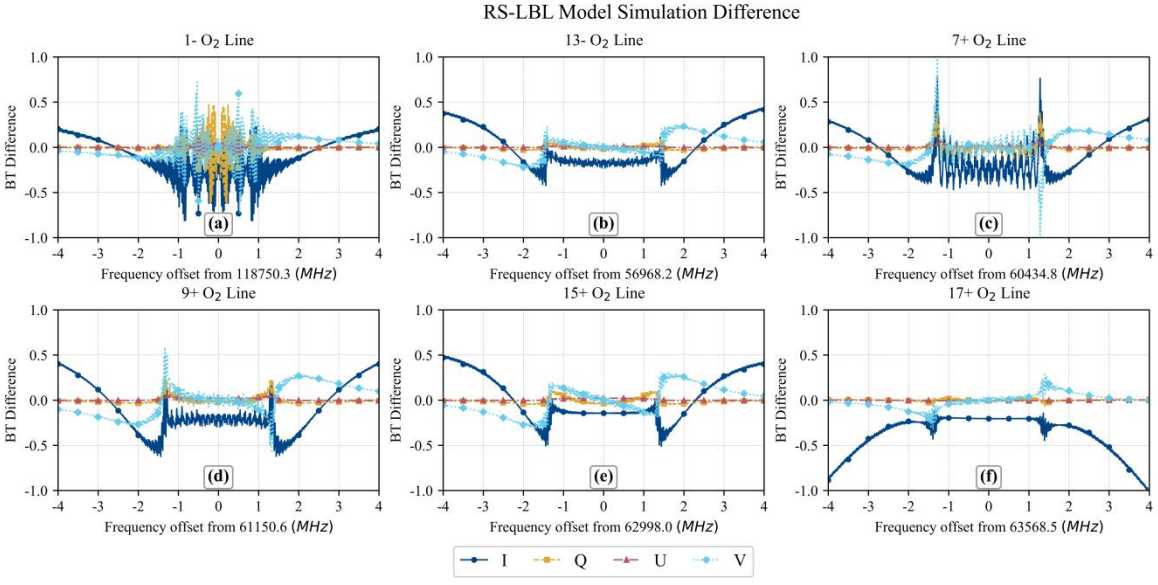

Figure 1: Stokes vector simulation differences between the Hund (b) and Larsson (2019) implementation of the microwave LBL model for total magnetic field strength Be = 0.5 Gauss, θ = 135°: (**a**) 1^- (118.7503 GHz); (**b**) 13^-(56.9682 GHz); (**c**) 7^+ (60.4348 GHz); (**d**) 9^+ (61.1506 GHz); (**e**) 15^+ (62.9980 GHz); and (**f**) 17^+ (63.5685 GHz) line (The dark blue (solid) line represents I, yellow (dashed) line represents Q, red (dashed-dotted) line represents U, and light blue (dotted) lines for V).

Considering that $g_{J_N}^{\text{Larsson}}$ primarily affects simulations at low J_N energy levels, where the 7^+ line intensity is the strongest, and the 1^- line occupies a unique frequency position, these two lines are simulated using the RS-LBL model (version 1988) with improved Larsson (2019) implementation. Figure 2 shows the BT matrix elements distribution for the 7^+ line and the 1^- line as a function of frequency for an input total magnetic field strength (B_e) of 0.5 Gauss, and θ of 135°. In Figures 2a and 2b, the BT matrix off-diagonal elements are used to describe the coherence of the diagonal elements. Figures 2c and 2d depict the BT matrix diagonal elements. From Figs. 2c and 2d, when the frequency offset between the 7^+ line and 1^- line is around 1 MHz, the circularly-based polarization BT is lower than that of the linearly-based. When the frequency shift exceeds 2 MHz, the brightness temperatures of circular and linear polarization are comparable. Additionally, the left-hand and right-hand circular polarization brightness temperatures are the mirror of one another at the oxygen line center. The horizontal and vertical linear polarization brightness temperatures are symmetric about the oxygen absorption line center frequency.

https://doi.org/10.5194/egusphere-2026-152
Preprint. Discussion started: 25 February 2026

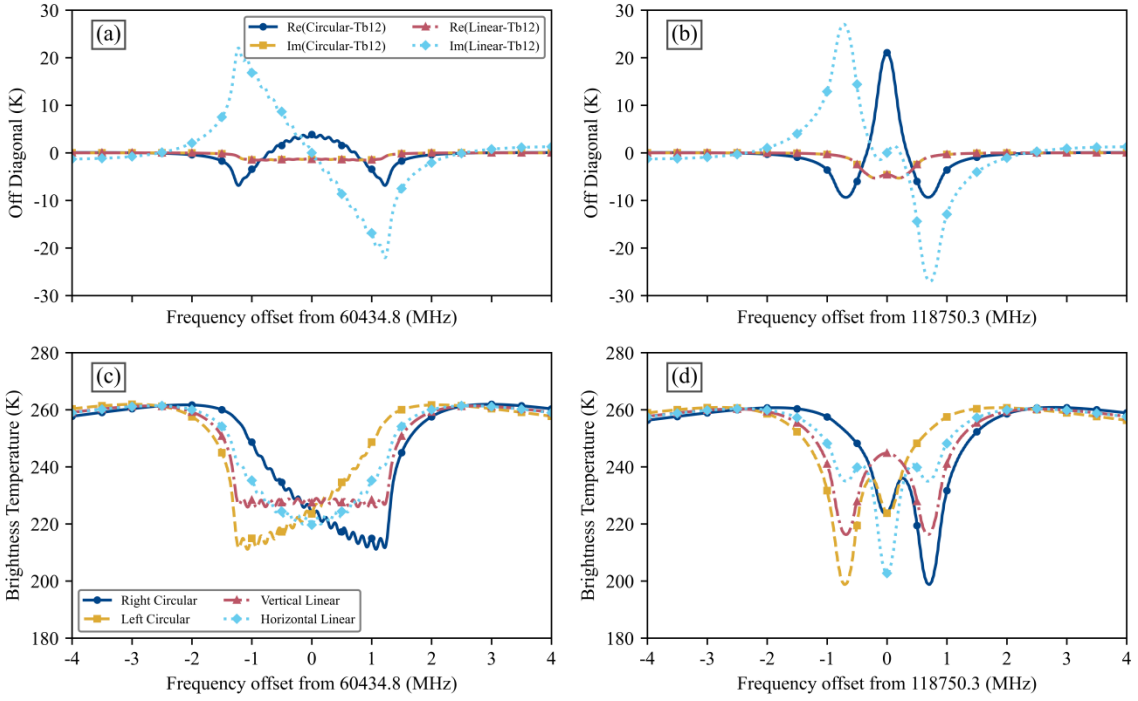

Figure 2: Brightness temperature matrix elements distribution as a function of frequency shift from 7^+ (left panel) and 1^- (right panel) line center. In (**a-b**), the dark blue (solid) and yellow (dashed) lines represent the real and imaginary parts of circular polarization, respectively, and the red (dashed-dotted) and light blue (dotted) lines represent the real and imaginary parts of linear polarization, respectively. In (**c-d**), the dark blue (solid) and yellow (dashed) lines represent the right-hand and left-hand circular polarization simulated BT, respectively, and the red (dashed-dotted) and light blue (dotted) lines represent the vertical and horizontal linear polarization BT, respectively.

3.2 Dependence of O_2 Line on Magnetic Field

To evaluate the impact of the Earth's magnetic field on O_2 absorption line simulations, two sets of experiments are conducted in this section. For experiment 1, the cosine of the angle between the magnetic field vector and the electromagnetic wave propagation direction ($\cos(\theta)$) is set to a fixed value of 0.7, while B_e increases from 0.2 to 0.7 Gauss in steps of 0.01 Gauss. For experiment 2, B_e is fixed at 0.45 Gauss, while θ ranges from 0° to 180° in steps of 1° ($\cos(\theta)$ from 1 to -1). Figure 3 shows the 7^+ line simulated brightness temperatures for different polarizations, with the y-axis representing frequency shift from line center increases from 0 to 5 MHz in steps of 1 MHz. From Fig. 3, at the frequency shift of approximately 2-3 MHz, a distinct high-temperature region (260-270 K) appears across the entire magnetic field, exhibiting a relatively uniform distribution. When the frequency shift exceeds 3 MHz, the BT exhibits a highly uniform horizontal distribution, indicating that the polarization state and magnetic field exert a negligible influence at high frequency shifts. However, when the frequency shift is below 2 MHz, the BT varies significantly with magnetic field strength, exhibiting unique behavior across different polarization states.

https://doi.org/10.5194/egusphere-2026-152
Preprint. Discussion started: 25 February 2026

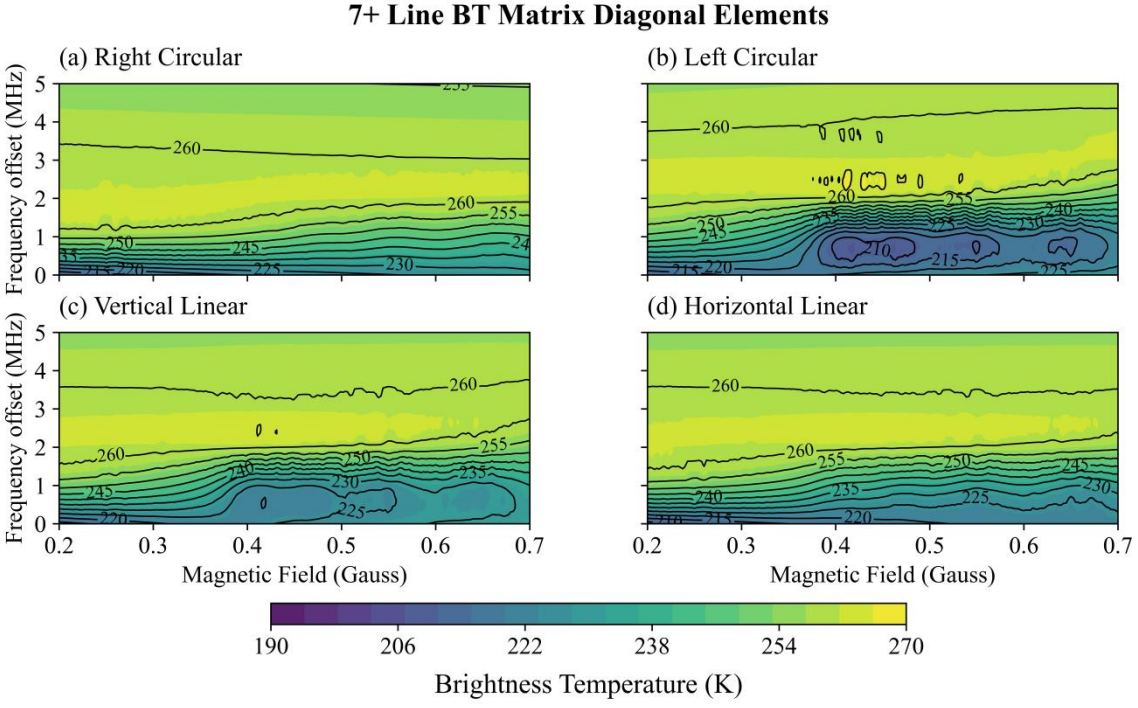

Figure 3: 7^+ line center frequency shift from 0-5 MHz (step of 1 MHz) simulated brightness temperature distribution with B_e from 0.2-0.7 Gauss (step of 0.01 Gauss) at a fixed $\cos(\theta)$ of 0.7 for (**a**) Right-hand circular polarization; (**b**) Left-hand circular polarization; (**c**) Vertical linear polarization; (**d**) Horizontal linear polarization.

The results of experiment 2 are presented in Fig. 4. Compared to the magnetic field strength distribution, the brightness temperature exhibits a more regular variation with θ. From Fig. 4a, the low-temperature region is primarily concentrated in the frequency shift below 1.5 MHz and a θ of 90°-180°, while the high-temperature region is mainly distributed in the frequency shift above 2 MHz. The left circular polarization (Fig. 4b) brightness temperature symmetry is to that of the right. Vertical linear polarization (Fig. 4c) shows low-temperature regions at frequency shifts below 1.5 MHz and within a θ range of 30°-150°, with the lowest temperature occurring near θ=90°. The horizontal linear (Fig. 4d) polarization brightness temperature shows good uniformity. When the frequency shift exceeds 1.5 MHz, the contour lines for linear polarization are nearly parallel to the x-axis, indicating that linear polarization detection has greater advantages under this condition. Additionally, the linear polarization BT is symmetric about θ=90°.

https://doi.org/10.5194/egusphere-2026-152
Preprint. Discussion started: 25 February 2026

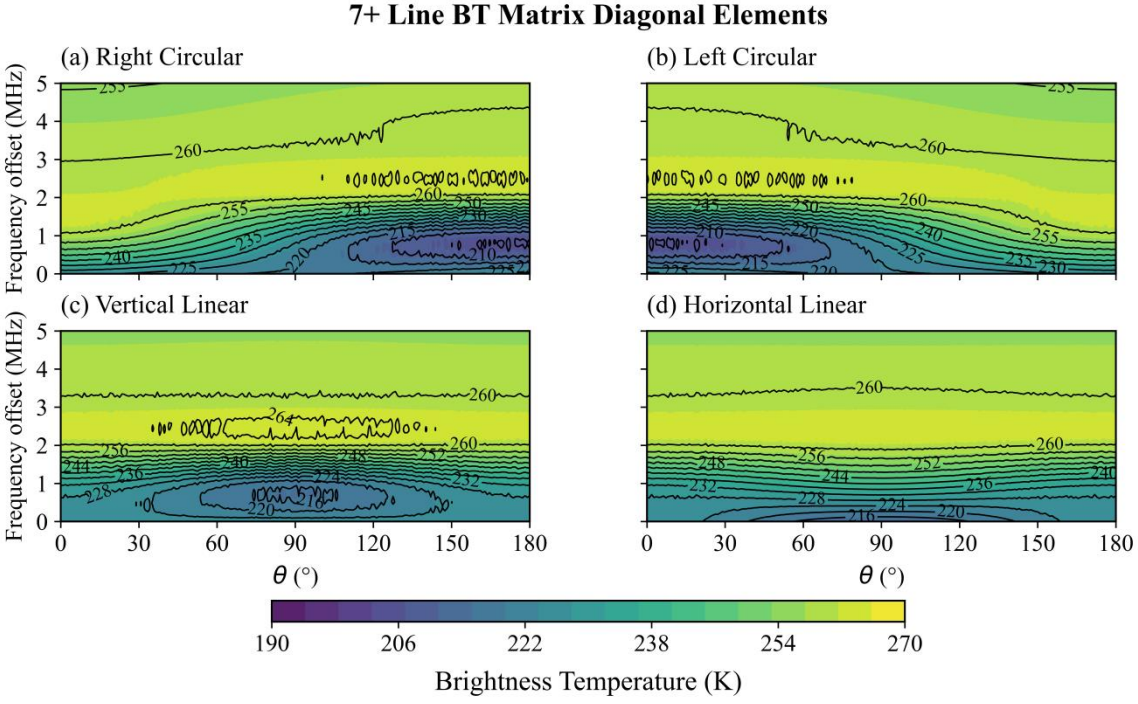

Figure 4: 7^+ line center frequency shift from 0-5 MHz (step of 1 MHz) simulated brightness temperature distribution with θ from 0-180° (step of 1°) at a fixed B_e of 0.45 Gauss for (**a**) Right-hand circular polarization; (**b**) Left-hand circular polarization; (**c**) Vertical linear polarization; (**d**) Horizontal linear polarization.

3.3 Analysis of Detection Altitude

Most past studies are based on fixed magnetic field strengths or angles, which are not sufficiently representative of the real Earth's atmospheric environment. This section performs three sets of cyclic calculations for B_e, θ, and frequency shift from the O_2 line center: 1. B_e ranges from 0.2-0.7 Gauss with steps of 0.1 Gauss. 2. θ ranges from 0° to 180° in steps of 1°. 3. The frequency is determined by a 10 MHz shift from the O_2 absorption line center in steps of 0.1 MHz. The detection altitude of the 50-70 GHz oxygen absorption line under varying frequency and magnetic field conditions is analyzed, providing theoretical support for designing microwave sounder channels in near space environments. 7^+ line vertical linear polarization BT is calculated and shown in Fig. 5, since past research focused more on circular polarization.

Each subplot of magnetic field strength in Fig. 5 displays two "peaks" (yellow high-BT) and one "valley" (purple low-BT). From Fig. 5, the "peaks" are primarily located near the 3 MHz frequency shift, with brightness temperatures reaching 260 K, while the "valleys" are mainly around the O_2 line center, with brightness temperatures as low as 220 K (corresponding to Fig. 3). When B_e increases from 0.2 Gauss to 0.7 Gauss, the "peaks" pattern remains virtually unchanged, but the "valleys" gradually contract upward, meaning that the brightness temperature upward with increasing magnetic field strength. The slope between "peak" and "valley" exhibits distinct temperature gradient variations (e.g., the boundary between yellow and

https://doi.org/10.5194/egusphere-2026-152
Preprint. Discussion started: 25 February 2026

orange), which are nearly unchanged with θ (consistent with the contour line structure in Fig. 4). This phenomenon indicates that the simulated brightness temperature increases with frequency shift and that the BT is unaffected by the observed angle. According to the standard atmospheric temperature profile distribution, the "peak" in Fig. 5 corresponds to an altitude of approximately 1 hPa. The simulated brightness temperature increases initially and then decreases with frequency shift, meaning the detection altitude gradually decreases.

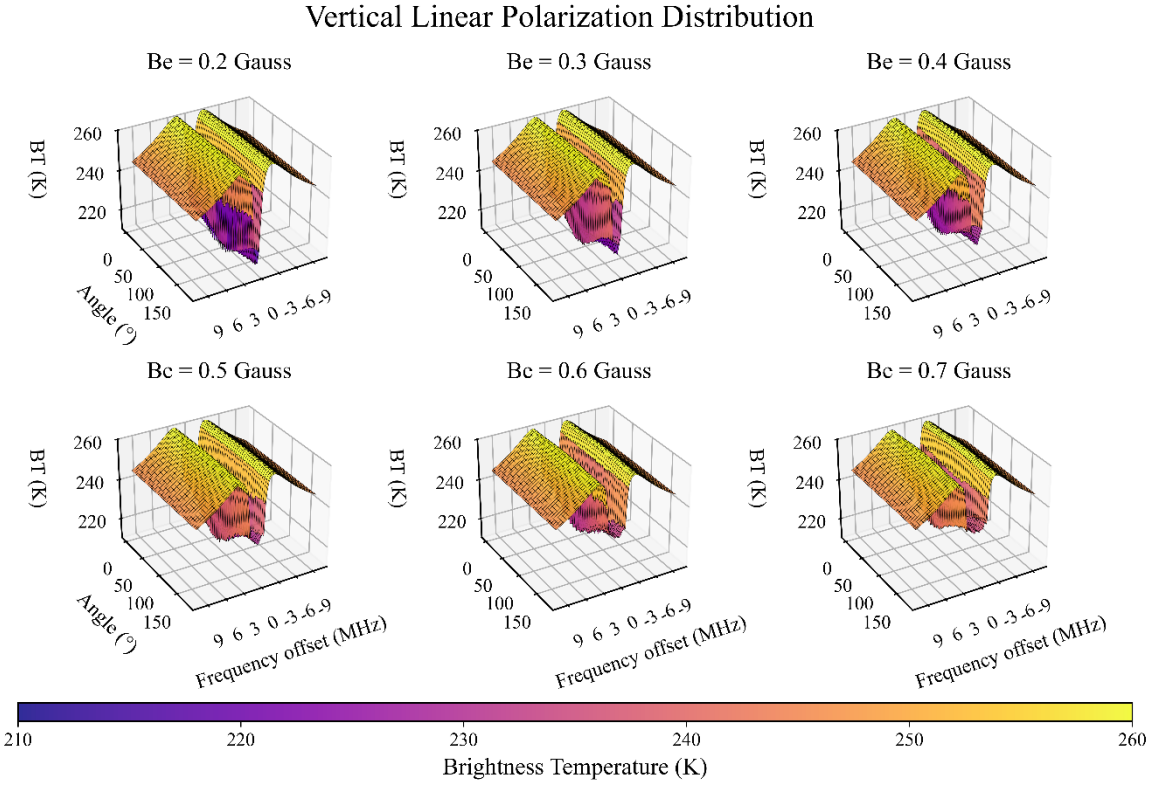

Figure 5: 7^+ line vertical linear polarization simulated brightness temperature distribution at 3 cyclic conditions: frequency shift of oxygen absorption line center from -10 MHz to 10 MHz in steps of 0.1 MHz, B_e ranges from 0.2-0.7 Gauss in steps of 0.1 Gauss, and θ ranges from 0° to 180° in steps of 1°.

When quantitatively analyzing detection altitude, weighting functions are typically employed, with the peak height corresponding to the altitude where the radiation signal is strongest (Zhang et al., 2024). The WF is typically defined as a function of single-layer (l) atmospheric pressure (P_l) and the transmittance at specific frequencies (v) (Rosenkranz and Staelin, 1988):

$$WF = \left(\Gamma_{l-1} - \Gamma_l\right) / \left[\ln\left(P_l\right) - \ln\left(P_{l-1}\right)\right] \tag{10}$$

when $l = 0$ (top of atmosphere):

$$WF = \left(1 - \Gamma_l\right) / \left[\ln\left(P_{l+1}\right) - \ln\left(P_l\right)\right] \tag{11}$$

https://doi.org/10.5194/egusphere-2026-152
Preprint. Discussion started: 25 February 2026

The avoidance of linear polarization in near space microwave remote sensing is largely due to its "double-peaked" WF (Rosenkranz and Staelin, 1988). According to Fig. 5, the locations where the WF exhibits "double-peaked" largely correspond to stronger magnetic field strength, meaning that linear polarization introduces uncertainty in observations and simulations of the polar regions or areas prone to electromagnetic storms. However, this "double-peaked" phenomenon changes with frequency shift. When the frequency shift exceeds 2 MHz, the magnetic field strength has a negligible effect on the temperature detection (Fig. 3). Furthermore, linear polarization offers significant symmetry advantages at the observed angle. It should be important for profiling the near space vertical atmosphere if the same oxygen absorption channel can be used for both linearly and circularly polarized detection.

To achieve full-polarization near space atmospheric detection, it is essential to investigate the distribution characteristics of the "double-peak" weighting function in linear polarization. The "double-peak" WF is more likely to appear at strong B_e (Fig. 5). Therefore, this study fixed the magnetic field strength and $\cos(\theta)$ at 0.63 Gauss and 0.9, respectively. The fine-structure weighting function for the 7^+ (60.4348 GHz) line and its 2 MHz frequency shift in 0.05 MHz is shown in Fig. 6. From Fig. 6, the WF is relatively narrow when the 7^+ line frequency shift is within 0.5 MHz, and the peak heights for both vertical (Figure 6a) and horizontal (Fig. 6e) polarization are approximately 60 km (0.1 hPa). The weighting function starts to broaden at frequency shift 0.75 MHz, gradually exhibiting "double-peaked". The altitudes of "double-peaked" are approximately 50 and 65 km, with the lower-level signal being stronger, particularly in horizontal polarization. The "double-peak" structure gradually weakens as the frequency shift continues to increase, and the WF signal of the lower atmosphere gradually intensifies. At a frequency shift of 2 MHz, it exhibits a perfect narrow "single-peaked" WF.

Therefore, for linear polarization, oxygen line frequency shifts outside the range of 0.8-1.8 MHz can be selected to avoid the effects of the "double peak". This selection of extreme cases aims to enable detailed simulation and analysis of oxygen lines under strong magnetic field conditions. Reality, not all oxygen absorption lines exhibit a "double peak" (such as 17^+) at high magnetic field strengths, which also depends on the intensity of the oxygen absorption line itself. In actual detection, multiple oxygen absorption lines are typically combined to diminish the influence of a single line.

https://doi.org/10.5194/egusphere-2026-152
Preprint. Discussion started: 25 February 2026

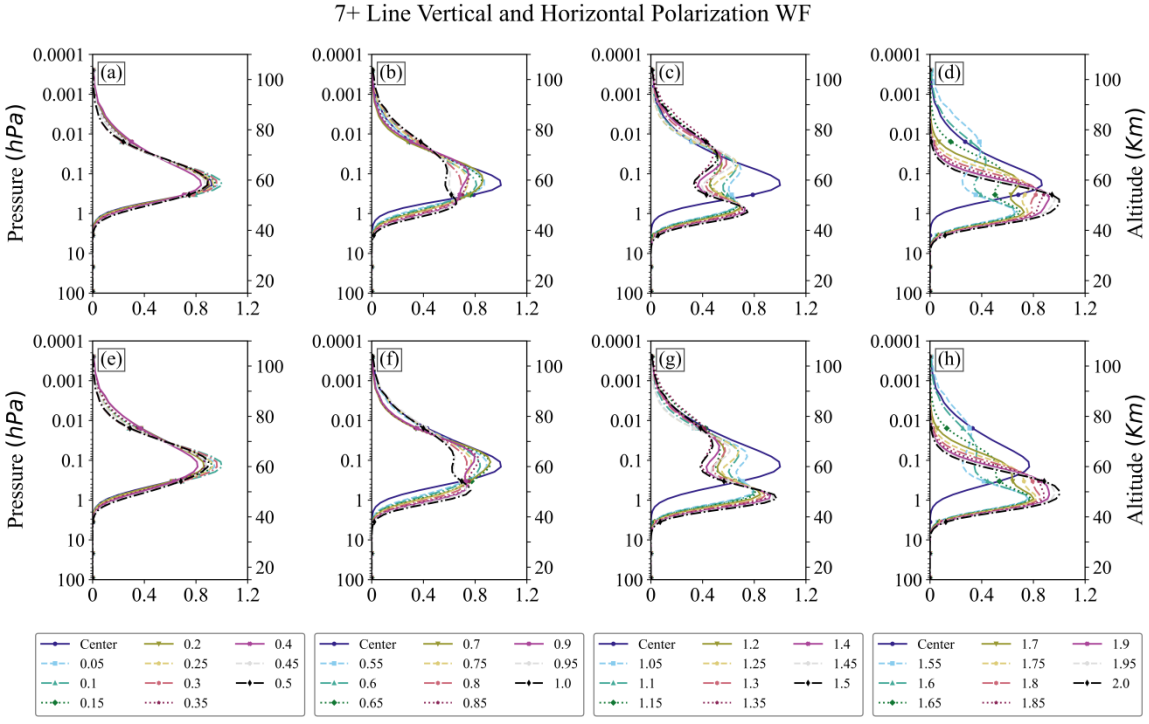

Figure 6: Weighting Functions of 7^+ line frequency shifts from 0.05-2 MHz at B_e of 0.63 Gauss and $\cos(\theta)$ of 0.9 for the (**a-d**) vertical linear polarization, and (**e-h**) horizontal linear polarization. (**a, e**) represent frequency shifts of 0.05-0.5 MHz from the 7^+ line center, (**b, f**) represent frequency shifts of 0.55-1.0 MHz, (**c, g**) represent shifts of 1.05-1.5 MHz, (**d, h**) represent shifts of 1.55-2.0 MHz. Colors denote the magnitude of the shift, with black lines indicating the 7^+ line.

4 Microwave Sounder in Near Space

4.1 SSMIS UAS Channel Characteristics

The SSMIS on board DMSP satellites, which features six channels capable of detecting altitudes from 20 to 100 km (Swadley et al., 2008). To achieve upper atmospheric detection, a narrow bandwidth is currently the preferred method (Lipton, 2003). However, a single narrow bandwidth often comes with significant channel noise, which may render the data unusable. The relationship between channel noise and bandwidth is as follows (Zhang et al., 2024):

$$NEDT = (T_r + T_a) / \sqrt{BW \cdot t} \tag{12}$$

where $NEDT$ denotes the channel noise, BW represents the channel bandwidth, T_r is the receiver equivalent noise temperature, T_a is the antenna temperature, and t is the integration time.

https://doi.org/10.5194/egusphere-2026-152
Preprint. Discussion started: 25 February 2026

To reduce noise, channels are typically designed as a double- or quadruple-sideband, and multi-line cooperative detection can significantly improve *NEDT* performance (Kunkee et al., 2008; Pardo et al., 1998). In SSMIS channel 19, the local oscillator (LO) is positioned between the 15^+ and 17^+ line frequencies, while channels 20-24 are between the 7^+ and 9^+ lines to achieve multiband detection. These UAS channels are designed for circular polarization. The SSMIS channel passband distribution is shown in Fig. 7. SSMIS channel 20 has two passbands with bandwidths of approximately 1.35 MHz covering the 7^+ and 9^+ lines, respectively. Channel 19 also features two passbands with bandwidths of approximately 1.35 MHz, covering the 15^+ and 17^+ lines, respectively. Channel 21 has four passbands, each bandwidth of approximately 1.3 MHz, positioned 2 MHz on either side of the 7^+ and 9^+ oxygen absorption lines. Channels 22-24 also feature four passbands centered at the 7^+ and 9^+ oxygen line frequencies, with frequency shifts of ±5.5 MHz, ±16 MHz, and ±50 MHz, respectively. Their respective bandwidths are 2.6 MHz, 7.35 MHz, and 26.5 MHz. The detection altitude of the channel decreases as the oxygen line shift increases, enabling detection of near space environments (Swadley et al., 2008).

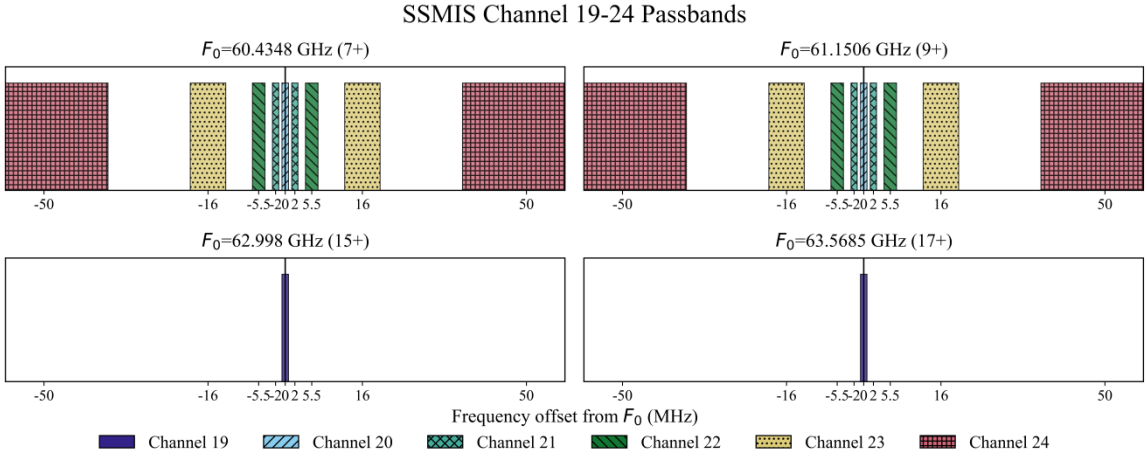

Figure 7: SSMIS channel 20-24 (upper panel) and channel 19 (bottom panel) passband distribution. The x-axis labels the passband frequency shift from the O_2 line, while the "rectangular" width indicates the bandwidth.

4.2 HMAS Passband Distribution

The SSMIS is relatively mature, with remaining instruments approaching the end of their operational lifetimes. This study proposes a high-resolution microwave sounder based on the same design principles as SSMIS, but with linear polarization. Aiming to increase near space observations, with the new channels complementing and extending the existing SSMIS UAS channels. To achieve high-resolution continuous detection, this study introduces channels that utilize new oxygen line combinations around 11^+ and 13^+ based on the existing channel specifications. The first channel bandwidth centered on each oxygen line is set to 1.8 MHz to reduce channel noise. Then a second channel with a bandwidth of 2 MHz is set near each further oxygen line offset of 1.9 MHz. Thanks to recent microwave hyperspectral detection technology, the channels away from the absorption line centers can all be set to narrow values, so the bandwidths of the remaining channels are all set to 2.2 MHz.

https://doi.org/10.5194/egusphere-2026-152
Preprint. Discussion started: 25 February 2026

Based on these design principles, multiple channels with narrow bandwidth can be formed on either side of the 7^+, 9^+, 11^+, 13^+, 15^+, and 17^+ oxygen lines. All these channel coverage or side of the oxygen absorption line can theoretically be implemented on the same instrument named Hyperspectral Microwave Atmospheric Sounder (HMAS). Figure 8 shows the HMAS partly channel distribution, where the top panel, middle panel, and bottom panel groups represent three sets of detection channels designed with different oxygen line combinations, with the corresponding passbands for the SSMIS channels overlaid. From Fig. 8, approximately 150 channels of the HMAS achieve continuous frequency coverage within the 7^+, 9^+, 11^+, 13^+, 15^+, and 17^+ oxygen line offsets to ±26 MHz with detection frequency from about 60-63 GHz.

To compare with SSMIS, the HMAS 150 channels are set to passband and combined into 39 composite channels. In HMAS 39 composite channels, there are 3 double-sideband and 36 quadruple-sideband composite channels. For microwave radiometers, the T_a is typically assumed to be 290 K, and the T_r is calculated based on frequency, approximately 300 K at 60 GHz (Zhang et al., 2024). In this study, the system noise temperature is set to 800 K ($T_r + T_a = 800\text{K}$). To reduce channel noise, we plan to extend the integration time to approximately 44.3 ms. According to Eq. (12), the *NEDT* of HMAS Composite Channel 1 is approximately 2 K. Table 1 gives the HMAS channel parameters.

Table 1 HMAS channel characteristics.

Channel	Center Frequency （GHz）	3-db Width（MHz）	NEDT（K）
1	60.7927±0.35790	1.8	2.00
2	60.7927±0.35790±0.0019	2.0	1.34
3	60.7927±0.35790±0.0040	2.2	1.28
4	60.7927±0.35790±0.0062	2.2	1.28
5	60.7927±0.35790±0.0084	2.2	1.28
6	60.7927±0.35790±0.0106	2.2	1.28
7	60.7927±0.35790±0.0128	2.2	1.28
8	60.7927±0.35790±0.0150	2.2	1.28
9	60.7927±0.35790±0.0172	2.2	1.28
10	60.7927±0.35790±0.0194	2.2	1.28
11	60.7927±0.35790±0.0216	2.2	1.28
12	60.7927±0.35790±0.0238	2.2	1.28
13	60.7927±0.35790±0.0260	2.2	1.28
14	62.1057±0.30550	1.8	2.00

https://doi.org/10.5194/egusphere-2026-152
Preprint. Discussion started: 25 February 2026

15	62.1057±0.30550±0.0019	2.0	1.34
16	62.1057±0.30550±0.0040	2.2	1.28
17	62.1057±0.30550±0.0062	2.2	1.28
18	62.1057±0.30550±0.0084	2.2	1.28
19	62.1057±0.30550±0.0106	2.2	1.28
20	62.1057±0.30550±0.0128	2.2	1.28
21	62.1057±0.30550±0.0150	2.2	1.28
22	62.1057±0.30550±0.0172	2.2	1.28
23	62.1057±0.30550±0.0194	2.2	1.28
24	62.1057±0.30550±0.0216	2.2	1.28
25	62.1057±0.30550±0.0238	2.2	1.28
26	62.1057±0.30550±0.0260	2.2	1.28
27	63.28325±0.28525	1.8	2.00
28	63.28325±0.28525±0.0019	2.0	1.34
29	63.28325±0.28525±0.0040	2.2	1.28
30	63.28325±0.28525±0.0062	2.2	1.28
31	63.28325±0.28525±0.0084	2.2	1.28
32	63.28325±0.28525±0.0106	2.2	1.28
33	63.28325±0.28525±0.0128	2.2	1.28
34	63.28325±0.28525±0.0150	2.2	1.28
35	63.28325±0.28525±0.0172	2.2	1.28
36	63.28325±0.28525±0.0194	2.2	1.28
37	63.28325±0.28525±0.0216	2.2	1.28
38	63.28325±0.28525±0.0238	2.2	1.28
39	63.28325±0.28525±0.0260	2.2	1.28

The integration time for the SSMIS channel 19-23 is 25.2 ms, and for channel 24 is 12.6 ms (Swadley et al., 2008). For comparison, the system noise is also set to 800 K when calculating the *NEDT* for SSMIS in this study. From Eq. (12), the SSMIS Channels 19-20 *NEDT* is approximately 3 K, which is highly consistent with the reported (2.7 K) (Kunkee et al., 2008). The number of channels and vertical resolution in this study are significantly higher than those of SSMIS, allowing for an appropriate extension of the integration time.

https://doi.org/10.5194/egusphere-2026-152
Preprint. Discussion started: 25 February 2026

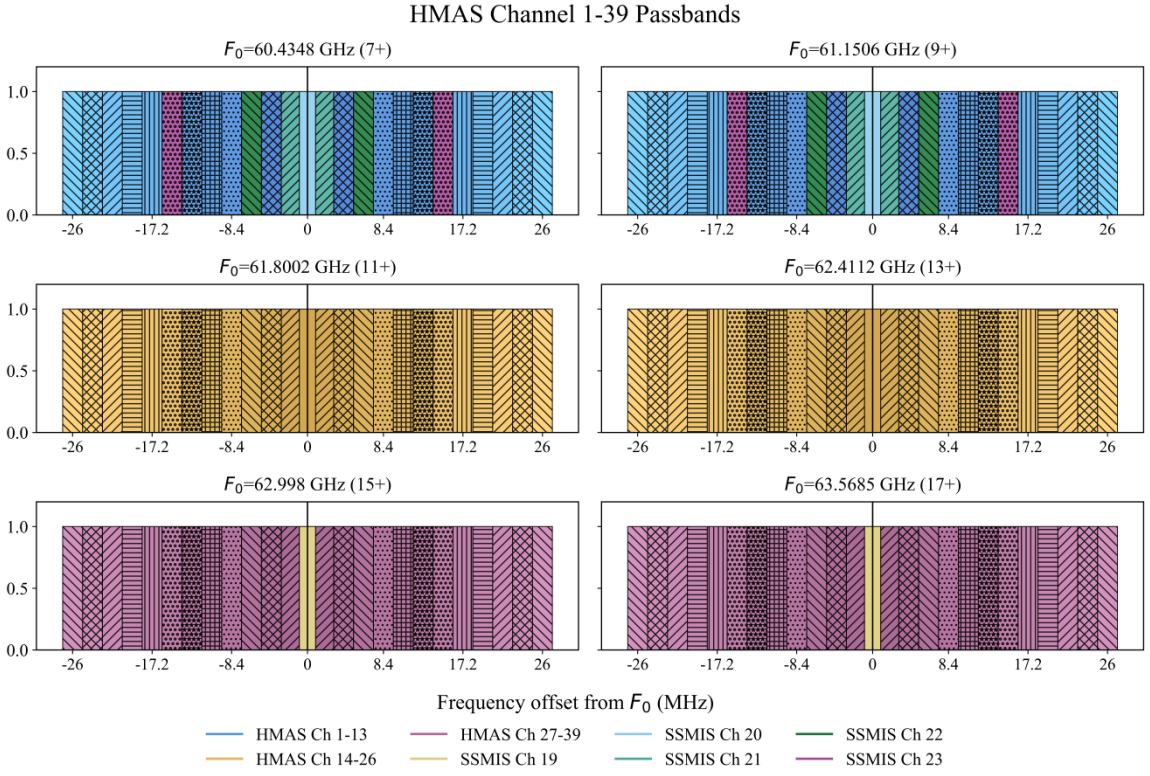

345 **Figure 8:** HMAS all-channel passband distribution. The orange, pink, bright green, dark blue, and purple lines in the 7^+, 9^+, 15^+, and 17^+ diagrams represent the SSMIS channels 19, 20, 21, 22, and 23 passbands, respectively.

Based on the same principle, high-resolution channels that do not utilize microwave hyperspectral detection technology are also proposed in this study. A double-sideband channel with a bandwidth of 1.8 MHz was set covering the oxygen absorption line. Four quadruple-sideband channels were established at frequencies progressively shifting away from the
350 absorption line center: 1.9 MHz, 4.0 MHz, 6.5 MHz, 9.9 MHz, 15.5 MHz, and 26 MHz, with respective bandwidths of 1.9 MHz, 2.1 MHz, 2.7 MHz, 3.9 MHz, 7.1 MHz, and 13.7 MHz. Table 2 gives the Microwave Atmospheric Sounder (MAS) channel parameters suitable for conventional detection techniques. This is essentially an extension of SSMIS channels 19-23, incorporating the 11^+ and 13^+ lines. However, the most significant difference between MAS and SSMIS is its capability to perform linear or circular polarization detection. The MAS can be manufactured with reference to the structure of ATMS or
355 AMSU to achieve end-to-end calibration.

Table2 MAS channel characteristics.

Channel	Center Frequency （GHz）	3-db Width（MHz）	NEDT（K）
1	60.7927±0.35790	1.8	2.00

https://doi.org/10.5194/egusphere-2026-152
Preprint. Discussion started: 25 February 2026

2	60.7927±0.35790±0.0019	1.9	1.38
3	60.7927±0.35790±0.0040	2.1	1.31
4	60.7927±0.35790±0.0065	2.7	1.16
5	60.7927±0.35790±0.0099	3.9	0.96
6	60.7927±0.35790±0.0155	7.1	0.71
7	60.7927±0.35790±0.0260	13.7	0.51
8	62.1057±0.30550	1.8	2.00
9	62.1057±0.30550±0.0019	1.9	1.38
10	62.1057±0.30550±0.0040	2.1	1.31
11	62.1057±0.30550±0.0065	2.7	1.16
12	62.1057±0.30550±0.0099	3.9	0.96
13	62.1057±0.30550±0.0155	7.1	0.71
14	62.1057±0.30550±0.0260	13.7	0.51
15	63.28325±0.28525	1.8	2.00
16	63.28325±0.28525±0.0019	1.9	1.38
17	63.28325±0.28525±0.0040	2.1	1.31
18	63.28325±0.28525±0.0065	2.7	1.16
19	63.28325±0.28525±0.0099	3.9	0.96
20	63.28325±0.28525±0.0155	7.1	0.71
21	63.28325±0.28525±0.0260	13.7	0.51

4.3 Comparison of SSMIS and HMAS

The atmospheric profile dataset used for SSMIS and HMAS simulation was developed by Peter Rayer (Met Office). It consists of 13,495 randomly sampled model profiles from the European Centre for Medium-Range Weather Forecasts (ECMWF), providing high vertical resolution (extending up to 0.0002 hPa). The key characteristics required for upper atmospheric simulations can be met by utilizing the average of this profile dataset. Figure 9 shows the HMAS weighting function distribution for different polarizations. The HMAS channels are grouped into three sets based on oxygen absorption line combinations: Group 1 (blue) comprises channels 1-13 centered around the 7^+ and 9^+ lines, Group 2 (yellow) includes channels 14-26 centered around the 11^+ and 13^+ lines, and Group 3 (pink) consists of channels 27-39 centered around the 15^+ and 17^+ lines. From Fig. 9, it is shown that the three double-sideband channels covering the respective oxygen absorption lines exhibit the highest peak with their respective WFs. Detection height gradually decreases as the passband moves further

https://doi.org/10.5194/egusphere-2026-152
Preprint. Discussion started: 25 February 2026

from the oxygen line center, with every 13 channels exhibiting a similar pattern. Using only channels 1-2, 14-15, and 27-28 enables detection at upper altitudes of approximately 40-80 km, while the remaining channels complete the high-resolution coverage of about 20-55 km.

The SSMIS UAS channel WFs are shown in Fig. 10 for different polarisations. The six-channel weighting functions also achieve similar coverage to HMAS from 100 hPa to 0.001 hPa. The SSMIS channel 24, with a center frequency shift of about 50 MHz, has a WF peak height of approximately 28 km (16 hPa). In contrast to SSMIS, the HMAS high-density weighting function is expected to provide rich atmospheric information in the near space.

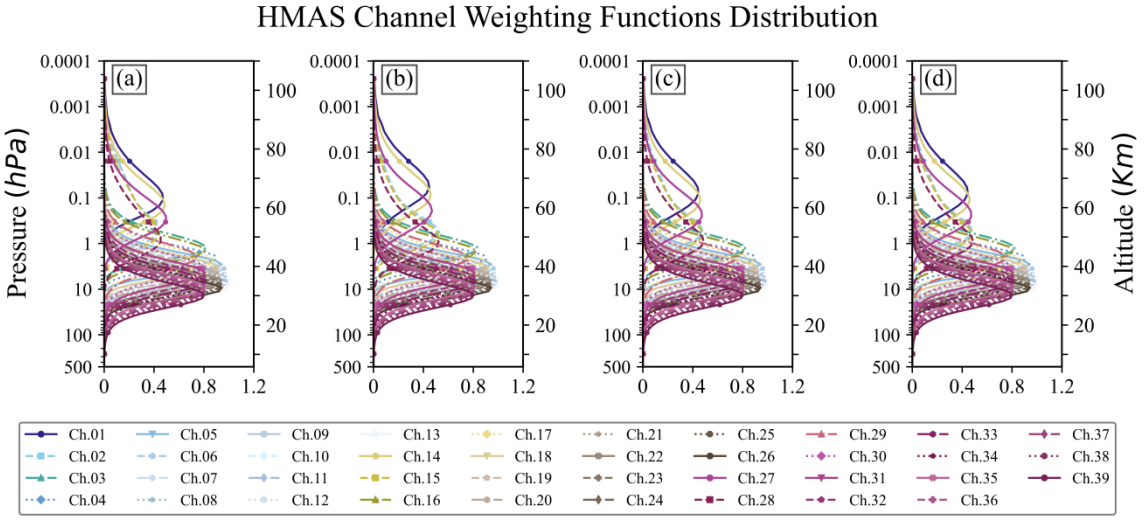

Figure 9: HMAS channel Weighting Functions (WF) for the (**a**) vertical-, (**b**) horizontal-, (**c**) right-, and (**d**) left-polarization. The first three channels in each group (channels 1-3, 14-16, and 27-29) are highlighted from the same color family.

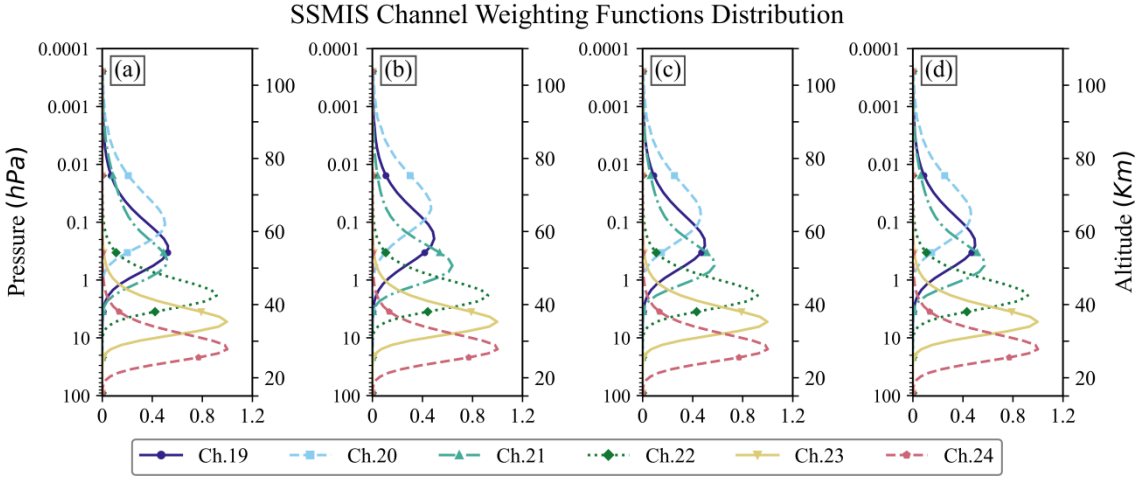

Figure 10: As Fig. 9, but for SSMIS channel 19-24.

https://doi.org/10.5194/egusphere-2026-152
Preprint. Discussion started: 25 February 2026

5 Conclusions

In this study, recent developments in the modelling of the Zeeman effect on high-peaking oxygen (O_2) absorption lines are incorporated into the microwave Line-by-Line (LBL) model to accurately simulate high-resolution satellite channels sensitive to these effects. The Stokes vector simulation differences for 1^-, 13^-, 7^+, 9^+, 15^+, and 17^+ oxygen absorption lines are compared, and it is shown that the 7^+ line has the largest simulation difference for the V component. Brightness temperature (BT) is simulated for representative 7^+ and 1^- oxygen lines using the Rosenkranz and Staelin's microwave Line-by-Line (RS-LBL) model updated with Larsson (2019) Zeeman splitting coefficients. The sensitivity of simulated BT to magnetic field strength (B_e) and angle between the magnetic field vector and the electromagnetic wave propagation direction (θ) indicates that the O_2 line center and frequency shift within 2 MHz are highly sensitive to B_e, particularly when it exceeds 0.4 Gauss, but above 2 MHz, there is negligible sensitivity. When the medium and magnetic field are uniformly distributed, and contributions from other absorption lines are neglected. The simulated BT exhibits symmetry with the θ, specifically, the linearly polarized BT of oxygen absorption lines is symmetric about θ=90° ($\cos(\theta)=0$), while left- and right-based circularly polarized BT are mirrors of each other.

The Special Sensor Microwave Imager Sounder (SSMIS) has six upper atmospheric sounding channels, which can potentially have a positive impact on assimilation (Hoppel et al., 2013). This study proposes both conventional and hyperspectral linear polarization channels parameters based on the simulation and analysis of oxygen absorption lines, aiming to complement and extend the capability of existing SSMIS observations, particularly as it reaches the end of its life. The channel configurations for both Hyperspectral Microwave Atmospheric Sounder (HMAS) and Microwave Atmospheric Sounder (MAS) are comparable to SSMIS, featuring double-sideband covering the oxygen line and quadruple-sideband channels on either side of the oxygen absorption line. To reduce channel noise, the bandwidth covering oxygen lines has been appropriately broadened. The study concludes by presenting the SSMIS and HMAS composite channel weighting function (WF) distributions. Overall, both the SSMIS and HMAS WFs achieve coverage from 100 to 0.001 hPa, but HMAS has a higher density, hence supported by hyperspectral detection technology, an instrument like HMAS is expected to obtain super high-resolution vertical atmospheric information from near space.

Since this study only focuses on the HMAS 150 channels at 60-63 GHz, with additional channels awaiting investigation. Meanwhile, the HMAS channel configuration is a conservative adaptation of existing techniques. In the future, channel setups can be fully adjusted based on technological capabilities, though all require simulation and analysis of the O_2 fine-structure line. Temperature profile retrieval based on current channel parameters also enables comparison of differences between HMAS or MAS and SSMIS.

https://doi.org/10.5194/egusphere-2026-152
Preprint. Discussion started: 25 February 2026

Code availability

The microwave LBL code used in this article can be downloaded at: https://cetemps.aquila.infn.it/mwrnet/lblmrt_ns.html.

Author contributions

CD and FW conceptualized and designed the experiments. CD, FW, and ET developed the methodology and performed the formal analysis, software development, data curation, and visualization. CD carried out the investigation and wrote the original draft. FW supervised the work and acquired funding. All co-authors contributed to writing, reviewing, and editing the final manuscript.

Competing interests

The authors declare no conflicts of interest.

Disclaimer

Copernicus Publications remains neutral with regard to jurisdictional claims made in the text, published maps, institutional affiliations, or any other geographical representation in this paper. While Copernicus Publications makes every effort to include appropriate place names, the final responsibility lies with the authors. Views expressed in the text are those of the authors and do not necessarily reflect the views of the publisher.

Financial support

This research was supported by the Hunan Provincial Natural Science Foundation of China (grant no. 2021JC0009); by the Natural Science Foundation of China (grant no. U2142212 and 42105136); by the Fengyun Application Pioneering Project (FY APP).

Review statement

The review statement will be added by Copernicus Publications listing the handling editor as well as all contributing referees according to their status anonymous or identified.

https://doi.org/10.5194/egusphere-2026-152
Preprint. Discussion started: 25 February 2026

References

Aires, F., Prigent, C., Orlandi, E., Milz, M., Eriksson, P., Crewell, S., Lin, C., and Kangas, V.: Microwave hyperspectral measurements for temperature and humidity atmospheric profiling from satellite: The clear-sky case, JGR Atmospheres, 120, https://doi.org/10.1002/2015JD023331, 2015.

Ben-Reuven, A. and Lightman, A.: Impact Broadening of the Oxygen Microwave Spectrum, The Journal of Chemical Physics, 46, 2429–2430, https://doi.org/10.1063/1.1841051, 1967.

Berdyugina, S. V. and Solanki, S. K.: The molecular Zeeman effect and diagnostics of solar and stellar magnetic fields: I. Theoretical spectral patterns in the Zeeman regime, A&A, 385, 701–715, https://doi.org/10.1051/0004-6361:20020130, 2002.

Bi, Y., Yang, J., Wei, C., Dou, F., Xu, W., An, D., Luan, Y., Feng, J., and Zhang, L.: Atmospheric Temperature Measurements Using Microwave Hyper-Spectrum from Geostationary Satellite: Band Design, Weighting Functions and Information Content, Remote Sensing, 16, 289, https://doi.org/10.3390/rs16020289, 2024.

Blackwell, W. J., Bickmeier, L. J., Leslie, R. V., Pieper, M. L., Samra, J. E., Surussavadee, C., and Upham, C. A.: Hyperspectral Microwave Atmospheric Sounding, IEEE Trans. Geosci. Remote Sensing, 49, 128–142, https://doi.org/10.1109/TGRS.2010.2052260, 2011.

Boukabara, S.-A. and Garrett, K.: Benefits of a hyperspectral microwave sensor, in: 2011 IEEE SENSORS Proceedings, 2011 IEEE Sensors, Limerick, Ireland, 1881–1884, https://doi.org/10.1109/ICSENS.2011.6127357, 2011.

Dong, C., Hu, H., and Weng, F.: Optimal Assimilation of Microwave Upper-Level Sounding Data in CMA-GFS, Adv. Atmos. Sci., 41, 2043–2060, https://doi.org/10.1007/s00376-024-3323-7, 2024.

Eckermann, S. D., Hoppel, K. W., Coy, L., McCormack, J. P., Siskind, D. E., Nielsen, K., Kochenash, A., Stevens, M. H., Englert, C. R., Singer, W., and Hervig, M.: High-altitude data assimilation system experiments for the northern summer mesosphere season of 2007, Journal of Atmospheric and Solar-Terrestrial Physics, 71, 531–551, https://doi.org/10.1016/j.jastp.2008.09.036, 2009.

Eckermann, S. D., Ma, J., Hoppel, K. W., Kuhl, D. D., Allen, D. R., Doyle, J. A., Viner, K. C., Ruston, B. C., Baker, N. L., Swadley, S. D., Whitcomb, T. R., Reynolds, C. A., Xu, L., Kaifler, N., Kaifler, B., Reid, I. M., Murphy, D. J., and Love, P. T.: High-Altitude (0–100 km) Global Atmospheric Reanalysis System: Description and Application to the 2014 Austral Winter of the Deep Propagating Gravity Wave Experiment (DEEPWAVE), Monthly Weather Review, 146, 2639–2666, https://doi.org/10.1175/MWR-D-17-0386.1, 2018.

https://doi.org/10.5194/egusphere-2026-152
Preprint. Discussion started: 25 February 2026

Eresmaa, R., Letertre-Danczak, J., Lupu, C., Bormann, N., and Mcnally, A. P.: The assimilation of Cross-track Infrared Sounder radiances at ECMWF, Quart J Royal Meteoro Soc, 143, 3177–3188, https://doi.org/10.1002/qj.3171, 2017.

Eriksson, P., Buehler, S. A., Davis, C. P., Emde, C., and Lemke, O.: ARTS, the atmospheric radiative transfer simulator, version 2, Journal of Quantitative Spectroscopy and Radiative Transfer, 112, 1551–1558, https://doi.org/10.1016/j.jqsrt.2011.03.001, 2011.

Hill, R. M. and Gordy, W.: Zeeman Effect and Line Breadth Studies of the Microwave Lines of Oxygen, Phys. Rev., 93, 1019–1022, https://doi.org/10.1103/PhysRev.93.1019, 1954.

Hoppel, K. W., Baker, N. L., Coy, L., Eckermann, S. D., McCormack, J. P., Nedoluha, G. E., and Siskind, E.: Assimilation of stratospheric and mesospheric temperatures from MLS and SABER into a global NWP model, Atmos. Chem. Phys., 2008.

Hoppel, K. W., Eckermann, S. D., Coy, L., Nedoluha, G. E., Allen, D. R., Swadley, S. D., and Baker, N. L.: Evaluation of SSMIS Upper Atmosphere Sounding Channels for High-Altitude Data Assimilation, Monthly Weather Review, 141, 3314–3330, https://doi.org/10.1175/MWR-D-13-00003.1, 2013.

Hui, A. K., Armstrong, B. H., and Wray, A. A.: Rapid computation of the Voigt and complex error functions, Journal of Quantitative Spectroscopy and Radiative Transfer, 19, 509–516, https://doi.org/10.1016/0022-4073(78)90019-5, 1978.

Koshelev, M. A., Vilkov, I. N., and Tretyakov, M. Yu.: Pressure broadening of oxygen fine structure lines by water, Journal of Quantitative Spectroscopy and Radiative Transfer, 154, 24–27, https://doi.org/10.1016/j.jqsrt.2014.11.019, 2015.

Koshelev, M. A., Vilkov, I. N., Makarov, D. S., Tretyakov, M. Yu., and Rosenkranz, P. W.: Speed-dependent broadening of the O 2 fine-structure lines, Journal of Quantitative Spectroscopy and Radiative Transfer, 264, 107546, https://doi.org/10.1016/j.jqsrt.2021.107546, 2021.

Kummerow, C. D., Poczatek, J. C., Almond, S., Berg, W., Jarrett, O., Jones, A., Kantner, M., and Kuo, C.-P.: Hyperspectral Microwave Sensors—Advantages and Limitations, IEEE J. Sel. Top. Appl. Earth Observations Remote Sensing, 15, 764–775, https://doi.org/10.1109/JSTARS.2021.3133382, 2022.

Kunkee, D. B., Poe, G. A., Boucher, D. J., Swadley, S. D., Hong, Y., Wessel, J. E., and Uliana, E. A.: Design and Evaluation of the First Special Sensor Microwave Imager/Sounder, IEEE Trans. Geosci. Remote Sensing, 46, 863–883, https://doi.org/10.1109/tgrs.2008.917980, 2008.

https://doi.org/10.5194/egusphere-2026-152
Preprint. Discussion started: 25 February 2026

Larsson, R., Buehler, S. A., Eriksson, P., and Mendrok, J.: A treatment of the Zeeman effect using Stokes formalism and its implementation in the Atmospheric Radiative Transfer Simulator (ARTS), Journal of Quantitative Spectroscopy and Radiative Transfer, 133, 445–453, https://doi.org/10.1016/j.jqsrt.2013.09.006, 2014.

Larsson, R., Lankhaar, B., and Eriksson, P.: Updated Zeeman effect splitting coefficients for molecular oxygen in planetary applications, Journal of Quantitative Spectroscopy and Radiative Transfer, 224, 431–438, https://doi.org/10.1016/j.jqsrt.2018.12.004, 2019.

Lenoir, W. B.: Propagation of Partially Polarized Waves in a Slightly Anisotropic Medium, Journal of Applied Physics, 38, 5283–5290, https://doi.org/10.1063/1.1709315, 1967.

Lenoir, W. B.: Microwave spectrum of molecular oxygen in the mesosphere, J. Geophys. Res., 73, 361–376, https://doi.org/10.1029/JA073i001p00361, 1968.

Liebe, H., Grimmestad, G., and Hopponen, J.: Atmospheric oxygen microwave spectrum--Experiment versus theory, IEEE Trans. Antennas Propagat., 25, 327–335, https://doi.org/10.1109/TAP.1977.1141573, 1977.

Liebe, H. J.: MPM?An atmospheric millimeter-wave propagation model, Int J Infrared Milli Waves, 10, 631–650, https://doi.org/10.1007/BF01009565, 1989.

Lipton, A. E.: Satellite sounding channel optimization in the microwave spectrum, IEEE Trans. Geosci. Remote Sensing, 41, 761–781, https://doi.org/10.1109/TGRS.2003.810926, 2003.

Liu, L., Bliankinshtein, N., Huang, Y., Gyakum, J. R., Gabriel, P. M., Xu, S., and Wolde, M.: Comparative experimental validation of microwave hyperspectral atmospheric soundings in clear-sky conditions, 2007.

Liu, Q., Kazumori, M., Han, Y., and Weng, F.: Calculating Antarctic stratospheric temperature from Special Sensor Microwave Imager and Sounder, Geophysical Research Letters, 34, 2007GL030646, https://doi.org/10.1029/2007GL030646, 2007.

Maurer, T., Ruston, B., Swadley, S., and Booton, A.: Assimilation Impacts of SSMIS Upper Atmosphere Soundings with Improved Orbital Bias Predictors in NAVGEM, 2015.

Mcnally, A. P., Watts, P. D., A. Smith, J., Engelen, R., Kelly, G. A., Thépaut, J. N., and Matricardi, M.: The assimilation of AIRS radiance data at ECMWF, Quart J Royal Meteoro Soc, 132, 935–957, https://doi.org/10.1256/qj.04.171, 2006.

https://doi.org/10.5194/egusphere-2026-152
Preprint. Discussion started: 25 February 2026

Meeks, M. L. and Lilley, A. E.: The microwave spectrum of oxygen in the Earth's atmosphere, J. Geophys. Res., 68, 1683–1703, https://doi.org/10.1029/JZ068i006p01683, 1963.

Nezlin, Y., Rochon, Y. J., and Polavarapu, S.: Impact of tropospheric and stratospheric data assimilation on mesospheric prediction, Tellus A, 61, 154–159, https://doi.org/10.1111/j.1600-0870.2008.00368.x, 2009.

Pardo, J. R., Gérin, M., Prigent, C., Cernicharo, J., Rochard, G., and Brunel, P.: REMOTE SENSING OF THE MESOSPHERIC TEMPERATURE PROFILE FROM CLOSE-TO-NADIR OBSERVATIONS: DISCUSSION ABOUT THE CAPABILITIES OF THE 57.5–62.5GHz FREQUENCY BAND AND THE 118.75GHz SINGLE O2 LINE, Journal of Quantitative Spectroscopy and Radiative Transfer, 60, 559–571, https://doi.org/10.1016/S0022-4073(97)00235-5, 1998.

Rosenkranz, P. W. and Staelin, D. H.: Polarized thermal microwave emission from oxygen in the mesosphere, Radio Science, 23, 721–729, https://doi.org/10.1029/rs023i005p00721, 1988.

Schadee, A.: On the Zeeman effect in electronic transitions of diatomic molecules, Journal of Quantitative Spectroscopy and Radiative Transfer, 19, 517–531, https://doi.org/10.1016/0022-4073(78)90020-1, 1978.

Stogryn, A.: The Magnetic Field Dependence of Brightness Temperatures at Frequencies Microwave Absorption, IEEE Trans. Geosci. Remote Sensing, 27, 279–289, https://doi.org/10.1109/36.17669, 1989.

Swadley, S. D., Poe, G. A., Bell, W., Ye Hong, Kunkee, D. B., McDermid, I. S., and Leblanc, T.: Analysis and Characterization of the SSMIS Upper Atmosphere Sounding Channel Measurements, IEEE Trans. Geosci. Remote Sensing, 46, 962–983, https://doi.org/10.1109/TGRS.2008.916980, 2008.

Tretyakov, M. Yu., Koshelev, M. A., Dorovskikh, V. V., Makarov, D. S., and Rosenkranz, P. W.: 60-GHz oxygen band: precise broadening and central frequencies of fine-structure lines, absolute absorption profile at atmospheric pressure, and revision of mixing coefficients, Journal of Molecular Spectroscopy, 231, 1–14, https://doi.org/10.1016/j.jms.2004.11.011, 2005.

Van Vleck, J. H.: The Absorption of Microwaves by Oxygen, Phys. Rev., 71, 413–424, https://doi.org/10.1103/PhysRev.71.413, 1947.

Van Vleck, J. H. and Weisskopf, V. F.: On the Shape of Collision-Broadened Lines, Rev. Mod. Phys., 17, 227–236, https://doi.org/10.1103/RevModPhys.17.227, 1945.

Weng, F.: Passive Microwave Remote Sensing of the Earth: for Meteorological Applications, 1st ed., Wiley, https://doi.org/10.1002/9783527336289, 2017.

https://doi.org/10.5194/egusphere-2026-152
Preprint. Discussion started: 25 February 2026

Yang, S., Yang, H., Li, N., and Ding, Z.: Short-Term Prediction of 80–88 km Wind Speed in Near Space Based on VMD–PSO–LSTM, Atmosphere, 14, 315, https://doi.org/10.3390/atmos14020315, 2023.

Zeeman, P.: XXXII. *On the influence of magnetism on the nature of the light emitted by a substance*, The London, Edinburgh, and Dublin Philosophical Magazine and Journal of Science, 43, 226–239, https://doi.org/10.1080/14786449708620985, 1897.

Zhang, M., Ma, G., He, J., and Zhang, C.: Impact of Channel Selection with Different Bandwidths on Retrieval at 50–60 GHz, Remote Sensing, 16, 1323, https://doi.org/10.3390/rs16081323, 2024.

Zhang, Y., Weng, F., and Hu, H.: Unraveling the Impacts of Hyperspectral Microwave and Terahertz Sounding Channels on Temperature and Humidity Profile Retrieval, J Meteorol Res, 39, 1088–1099, https://doi.org/10.1007/s13351-025-4042-4, 2025.

Zhao, X. R., Sheng, Z., Shi, H. Q., Weng, L. B., and He, Y.: Middle Atmosphere Temperature Changes Derived from SABER Observations during 2002-2020, Journal of Climate, 1, https://doi.org/10.1175/JCLI-D-20-1010.1, 2021.